CHARACTERISTICS OF INTERACTING PROCESS WITH HORSESHOE VORTEX AND LONGITUDINAL VORTEX

Takaaki Shizawa, Shinji Honami
Department of Mechanical Engineering, Science University of Tokyo
1-3 Kagurazaka Shinjyuku-ku, Tokyo 162-8601, Japan

Mamoru Takahashi
Takasago Machinery Works, Mitsubishi Heavy Industries, Ltd.
2-1-1 Arai Araimachi Takasago-shi, Hyogo 210-0862, Japan

Hiroyuki Hara
Power System Engineering Center, Mitsubishi Heavy Industries, Ltd.
3-3-1 Minatomirai Yokohama-shi, Kanagawa 220-8401, Japan

ABSTRACT

This paper presents the behavior of a passively controlled horseshoe vortex at the root of *NACA0024* wing, which is established on a turbulent boundary layer. A pair of vortex generators of half delta wing is installed upstream of the wing. The characteristics of optimally controlled case of interacting process with longitudinal vortex and horseshoe vortex are carefully investigated. In case of *Common Flow Up Configuration* of vortex generator, the horseshoe vortex is not shifted from the wing, because the longitudinal vortex is restrained. In case of *Common Flow Down Configuration*, the interacting vortex that has strong vorticity by a pairing process is shifted far away from the wing, and the paring occurs in a short distance.

INTRODUCTION

The turbulent flow at the root of a wing junction is very complex, highly three-dimensional, yet it is commonly encountered. A horseshoe vortex is observed at the junction of wing and wall. The vortex acts as if it would shorten the span of the wing, and then both total pressure loss and local heat transfer rate are increased. Therefore, it is undesirable phenomena for the wing.

The intensive studies about the horseshoe vortex by Shabaka and Bradshaw (1981), Mehta (1984) and Kubendran et al. (1986) made clear the structure of the horseshoe vortex. Eckerle and Awad (1991) studied the horseshoe vortex around the circular cylinder. Devenport and Simpson (1990) studied the separated flow immediately upstream of the leading edge of the idealized wing/body junction. Fleming et al. (1993) tested the effects of inlet boundary layer conditions of this type of flow and Shizawa et al. (1996) reported the effects of streamwise pressure gradient on horseshoe vortex.

On the other hand, a longitudinal vortex downstream of a vortex generator is conventionally used to control separation over the wing. Pauley and Eaton (1988) investigated extensively the characteristics of longitudinal vortex pairs. Shizawa and Eaton (1992) discussed the behavior of the longitudinal vortex in a three-dimensional turbulent boundary layer.

Now, we consider the cases that the longitudinal vortex pair by the *VG* (*Vortex Generator*) is interacting with the horseshoe vortex, as shown in Figure 1. In case of *CFUC* (*Common Flow Up Configuration*), the boundary layer thickness between the *VG* pair becomes thick. The direction of rotation of the longitudinal vortex and horseshoe vortex is the opposite in this case. On the other hand, The boundary layer thickness between the *VG* pair becomes thin in *CFDC* (*Common Flow Down Configuration*). The direction of rotation of each vortex is the same.

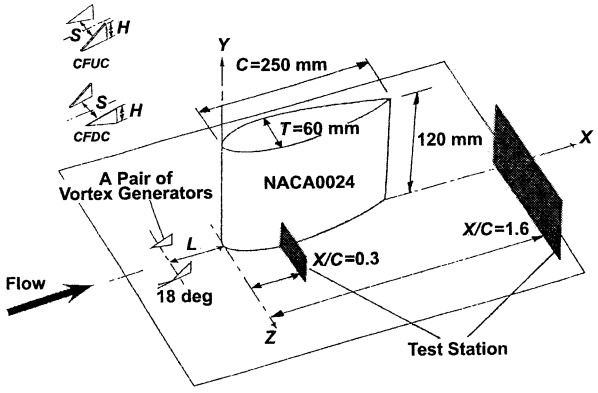

Fig. 1 Experimental setup (Dimensions in mm)

The objective of this paper is to control passively the horseshoe vortex by the longitudinal vortex pair. Then, both an optimum configuration of the *VG* pair and the characteristics of the interacting process are carefully investigated.

EXPERIMENTAL SETUP AND METHOD

Figure 1 presents a schematic drawing of the experimental setup. The return type wind tunnel has a cross section of 130 mm x 700 mm. The reference velocity *Ur* is 16.7 m/s and turbulent intensity is 0.15 %. The boundary layer thickness δ and momentum thickness δ_2 are 22.0 mm and 3.5 mm respectively, and the momentum thickness Reynolds number $Re_{\delta 2}$ is 2300 when the wing is not installed. The coordinate system employed is the wind tunnel coordinate and the origin is selected at the leading edge of the wing.

The cord length *C* of *NACA0024* wing is 250 mm and the span is 120 mm. The maximum thickness *T* is 60 mm at 30 % cord length. The wing is installed carefully into the wind tunnel with zero attack angle to the approaching flow.

The half delta wing type of *VG* has an attack angle of 18° to the approaching flow. The sizes of *VG* in the "*Optimum Case*" are *H/T* = 0.16 and *S/T* = 0.67. In the "*Base Case*", the sizes are *H/T* = 0.25 and *S/T* =0.67. The *VG* pair is installed in symmetric with respect to the wing centerline and *L/T* = 1.0 upstream of the leading edge of the wing. Now, *H* is the height, *S* is the spacing and *L* is the installed distance of *VG*. All distances about *VG* are measured from the center of the baseline of *VG*.

The wall flow pattern is tested by an oil film flow visualization and wall static pressure is measured. A three-hole Pitot probe is used to measure the total pressure loss. An *X*-array hot-wire anemometer is used to measure the turbulent energy and Reynolds shear stress. The test stations are at *X/C* = 0.3 and *X/C* = 1.6 of hatched *Y–Z* section in Figure 1.

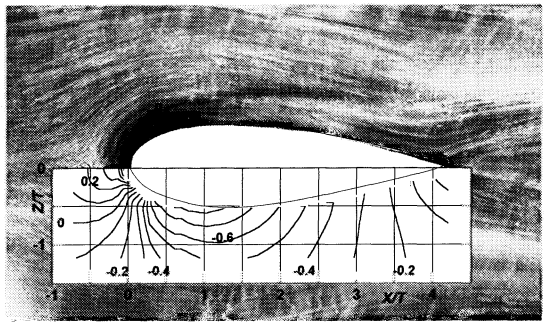

(a) non-*VG*

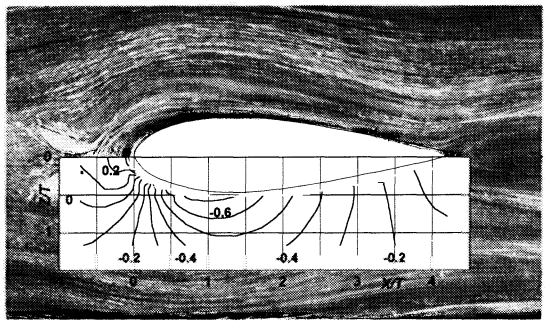

(b) *CFUC*

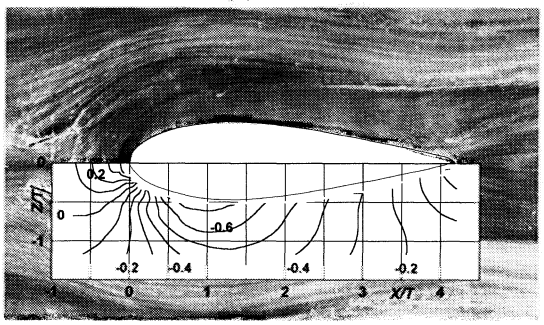

(c) *CFDC*

Fig. 2 Wall flow pattern and wall static pressure

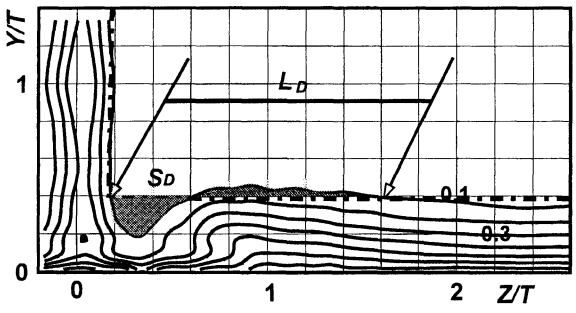

(a) non-*VG*

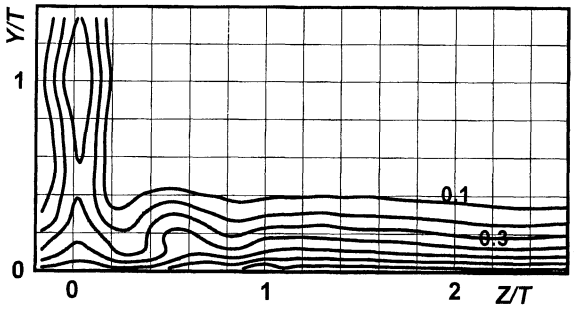

(b) *CFUC* (*H/T* = 0.17, *S/T* = 0.67)

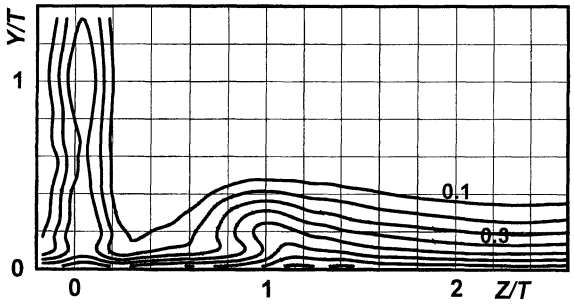

(c) *CFDC* (*H/T* = 0.17, *S/T* = 0.67)

Fig. 3 Contours of total pressure C_{pt} (*X/C* = 1.6)

RESULTS AND DISCUSSIONS

Wall Flow Pattern and Total Pressure Loss

Figure 2 presents the wall flow pattern and wall static pressure coefficient C_{ps}. Figure 2(a) shows the non-*VG* case and the separation line and the line of low mean wall shear stress by the horseshoe vortex are clearly observed. In base case of *CFUC*, as shown in Figure 2(b), the separation line is not observed. On the other hand, the line of low mean wall shear stress is observed close to the wing. All streak lines present non-disturbed smooth flow pattern along the wing. The location of maximum peak of each C_{ps} contour near the leading edge is shifted toward downstream compared with non-*VG* case. In base case of *CFDC*, as shown in Figure 2(c), the wall flow pattern presents the strong effects of the interacting vortex. Both lines are located almost parallel to *X*–axis away from the wing.

Figure 3 presents the contours of total pressure loss coefficient C_{pt} at X/C = 1.6. In case of non-*VG*, as shown in Figure 3(a), the footprint of the horseshoe vortex is shown as distortion of the contours away from the wing. In optimally controlled case of *CFUC*, the smoother contours are observed, as shown in Figure 3(b). Therefore, the total pressure loss at the root of the wing becomes large. In optimally controlled case of *CFDC*, as shown in Figure 3(c), the secondary flow is dominant and fluid with low total pressure loss penetrates into the root of the wing.

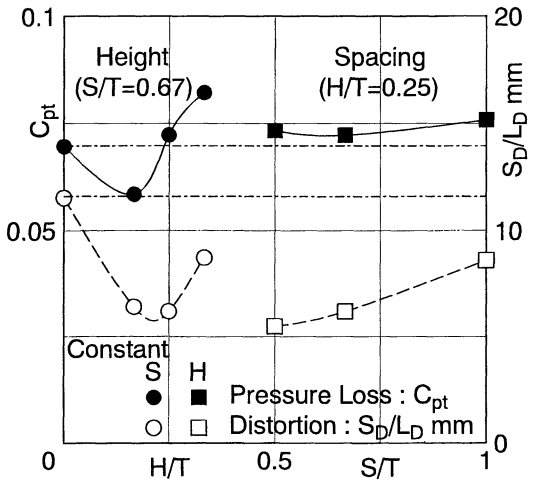

(a) *CFUC*

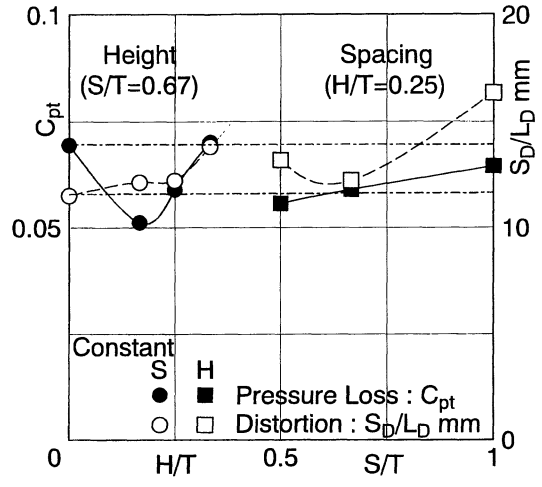

(b) *CFDC*

Fig. 4 Distortion and total pressure loss (X/C = 1.6)

Mass Flow Averaged C_{pt} and Distortion

To evaluate above results quantitatively, Figure 4(a) presents distortion of C_{pt} contours and mass flow averaged $\overline{C_{pt}}$ with the change in the height and the spacing of *VG* in

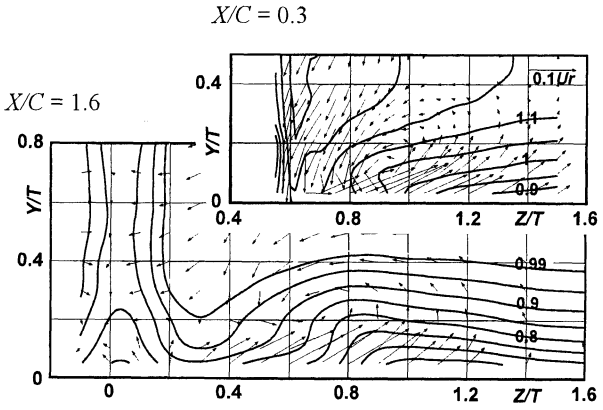

(a) non-*VG*

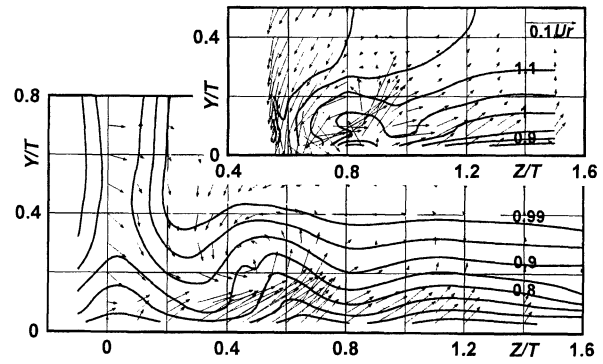

(b) *CFUC* (H/T = 0.17, S/T = 0.67)

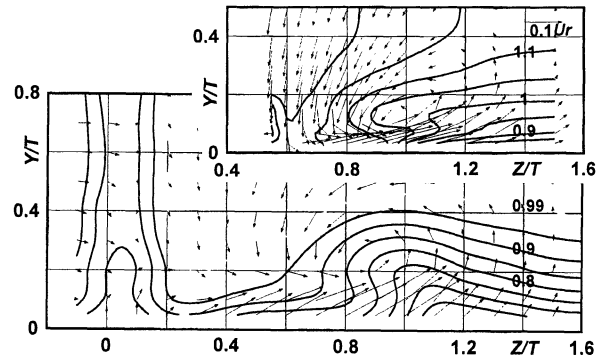

(c) *CFDC* (H/T = 0.17, S/T = 0.67)

Fig. 5 *U* Contours and secondary flow vector

case of *CFUC*. Distortion is defined as the area of S_D and normalized the distance L_D, as shown in Figure 3(a). Both the total pressure loss and distortion have a minimum peak, and the sizes of height and spacing of *VG* are the optimum. Distortion is diminished by 49 % and the total pressure loss is diminished by 17 % of non-*VG* case. On the other hand, as shown in Figure 4(b), distortion increases monotonically with increase in height, in case of *CFDC*. The total pressure loss decreases at all cases. In an optimally controlled case, the total pressure loss is decreased by 29 % of non-*VG* case.

The smaller distortion in C_{pt} contours without extreme total pressure loss is expected in case of *CFUC*, although the margin to optimum height of *VG* is narrow. The low total pressure loss is expected at the root of the wing, in case of *CFDC*.

Mean Velocity and Secondary Flow Vector

Figures 5(a) to 5(c) present the mean velocity and secondary flow vector at X/C = 0.3 and 1.6. Figure 5(a) shows the non-*VG* case. The contours show a positive slope in Z–direction, because the flow is accelerated at X/C = 0.3. The secondary flow vector presents the existence of counter-clockwise horseshoe vortex at a distance from the wing. The center of the vortex (Y/T, Z/T) is located at (0.12, 0.92) at X/C =0.3 and (0.25, 0.65) at X/C = 1.6, respectively.

Figure 5(b) presents the optimally controlled *CFUC* case. The high-speed region is observed at Z/T = 0.95 of X/C = 1.6. The region corresponds to the longitudinal vortex by the vorticity profile, as shown in Figure 6(b). The low speed region near the wing corresponds to the horseshoe vortex. The direction of rotation of longitudinal vortex and horseshoe vortex is opposite each other, but the velocity vector exhibits a counter-clockwise vortex. The center of interacting vortex is (0.15, 0.8) at X/C = 0.3 and (0.25, 0.45) at X/C = 1.6. The center of the interacting vortex is shifted toward the wing.

Figure 5(c) shows the optimally controlled *CFDC* case. The velocity contours present the same profile as non-*VG* case. The direction of rotation of longitudinal vortex is the same as horseshoe vortex. The center of interacting vortex is (0.3, 0.9) at X/C = 0.3 and (0.3, 0.9) at X/C = 1.6. The distance between the center of interacting vortex and wing is large in this case. The large downwash vector is also observed in this case. Therefore, the wider region of high momentum flow is observed between wing and interacting vortex.

Streamwise Vorticity

Figures 6(a) to 6(c) present the streamwise mean vorticity Ω_x contours normalized by the reference velocity U_r and the maximum thickness of wing T at X/C = 1.6. The solid line exhibits the negative vorticity looking downstream.

In case of optimally controlled *CFUC*, the area of interacting vortex is decreased by 55 % of non-*VG* case, as shown in Figure 6(b). The smaller area of positive vorticity (dot-dashed line) by the longitudinal vortex is observed at Z/T = 0.75.

Figure 6(c) presents the *CFDC* of optimally controlled case. The maximum vorticity of the interacting vortex is large compared with non-*VG* case. The location of peak vorticity is shifted away from the wing.

In case of *CFUC*, the direction of rotation of longitudinal vortex and horseshoe vortex is opposite. Furthermore, these vortices have an unequal strength. The horseshoe vortex is restricted to move toward the spanwise direction by longitudinal vortex. Therefore, the vortex moves downstream along the wing. The dominant vorticity of the interacting vortex has the same sign with horseshoe vortex. The vorticity of the longitudinal vortex is weak and the size and vorticity of the longitudinal vortex are decided by the height and the spacing of the *VG*.

In case of *CFDC*, longitudinal vortex and horseshoe vortex have the same direction of rotation. The interacting vortex has the large maximum vorticity and stretched in the spanwise direction as the results of pairing process. But the pairing process occurs about 52 % shorter distance compared with the result of *Co-rotating Configuration* by Pauley and Eaton (1988). As

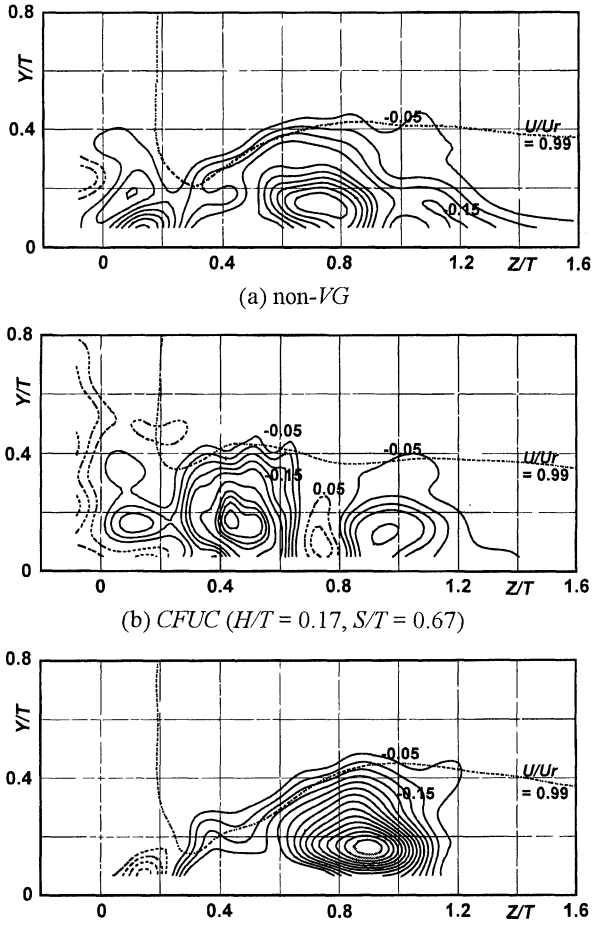

(a) non-*VG*

(b) *CFUC* (H/T = 0.17, S/T = 0.67)

(c) *CFDC* (H/T = 0.17, S/T = 0.67)

Fig. 6 Contours of streamwise vorticity $\Omega_x T/U_r$ (X/C = 1.6)

the interacting vortex has the strong vorticity compared with the non-*VG* case, the interacting vortex is shifted farther away from the wing as the results of mirror vortex with respect to the wing.

Turbulent Kinetic Energy q^2

Figures 7(a) to 7(c) present the turbulence energy q^2 contours at X/C = 1.6. The contours of turbulent kinetic energy show large value at the vortex core and the upwash region of the secondary flow. Therefore, the maximum peak of turbulent kinetic energy is located away from the center of interacting vortex both Y and Z–direction. The contours show large value at almost the same location of high total pressure loss, as shown in Figure 3.

Turbulent Shear Stress $-\overline{uv}$

Figures 8(a) to 8(c) show the Reynolds shear stress $-\overline{uv}$ contours at X/C = 1.6. In case of non-*VG*, as shown in Figure 8(a), the profile shows positive contours at upwash region of the secondary flow. The narrower region of negative shear stress is observed close to the wall.

Figure 8(b) presents the complex shear stress contours in *CFUC*. It shows negative value close to the wall and positive value at upwash region of the interacting vortex. As shown in Figure 6(b), the interacting vortex is classified into *Unequal Strength Common Flow Up Configuration*. The weaker vorticity of the longitudinal vortex is merged into the stronger vorticity of the horseshoe vortex. Therefore, the positive contours from Z/T = 0.3 to 0.9 are closed.

In case of *CFDC*, as shown in Figure 8(c), the shear stress shows large value at upwash region of secondary flow as the results of the pairing process. The peak has a large value compared with non-*VG* case and is located away from the wing.

Characteristics of Vorticity at X/C = 0.3

The weaker vorticity of longitudinal vortex and the narrower margin of optimum height of *VG* are reported in case of *CFUC*. On the other hand, the rapid pairing process of longitudinal vortex and horseshoe vortex is observed in case of *CFDC*. In order to make clear the interacting process, Figure 9 presents the vorticity at X/C =0.3. The area of interacting vortex is defined as the contour bounds larger than the absolute value of 0.5.

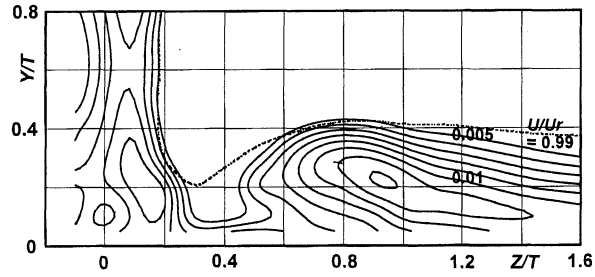

(a) non-*VG*

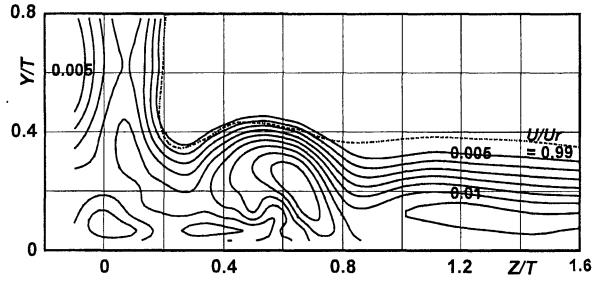

(b) *CFUC* (*H/T* = 0.17, *S/T* = 0.67)

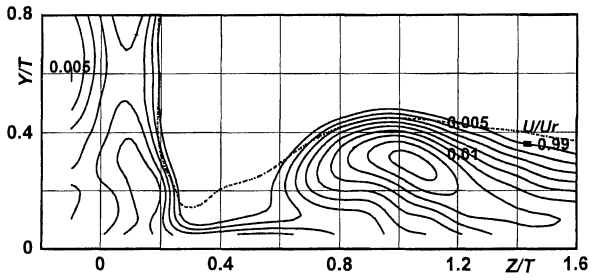

(c) *CFDC* (*H/T* = 0.17, *S/T* = 0.67)

Fig. 7 Contours of turbulence energy q^2/Ur^2 (X/C = 1.6)

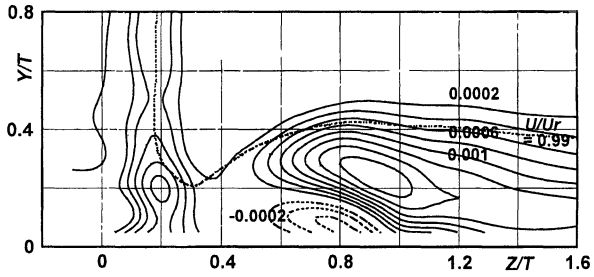

(a) non-*VG*

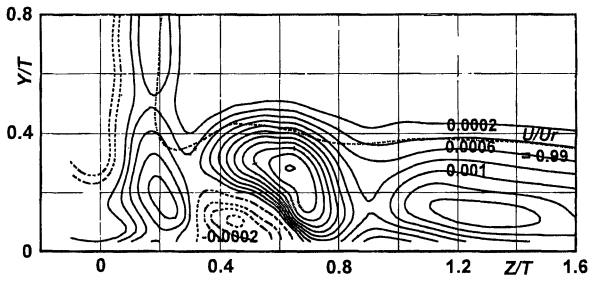

(b) *CFUC* (*H/T* = 0.17, *S/T* = 0.67)

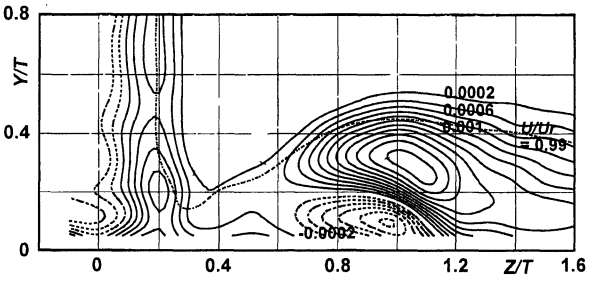

(c) *CFDC* (*H/T* = 0.17, *S/T* = 0.67)

Fig 8 Contours of $-\overline{uv}/U_r^2$ (X/C = 1.6)

Figure 9(b) shows the optimally controlled *CFUC* case. The region of dot-dash line (positive vorticity by longitudinal vortex) is observed next to that of the solid line (negative vorticity by horseshoe vortex). The area of interacting vortex is decreased by 80 % of non-*VG* case (Figure 9(a)). A key point of optimally controlled case is that the weaker vorticity of the longitudinal vortex than the horseshoe vortex is provided.

In case of *CFDC*, as shown in figure 9(c), the area of interacting vortex is increased by 150 % of non-*VG* case. The direction of rotation is the same as horseshoe vortex, and the pairing process of the two vortices is already completed.

CONCLUSIONS

The horseshoe vortex is passively controlled by a pair of vortex generators installed upstream of the wing. Following conclusions are obtained.

(1) In case of *Common Flow Up Configuration*, the interacting vortex shifts toward the root of the wing. Distortion of total pressure loss contours is decreased by 49 % of non-*VG* case.

(2) In case of *Common Flow Down Configuration*, the interacting vortex shifts further away from the wing by the mirror vortex with respect to the wing. The interacting vortex has a strong vorticity by pairing process and the pairing process occurs in a short distance. The total pressure loss is decreased by 29 % of non-*VG* case.

(3) Turbulent kinetic energy shows large value at the region with high total pressure loss.

(4) In the optimally controlled case in *Common Flow Up Configuration*, the weaker vorticity of the longitudinal vortex than the horseshoe vortex is provided. The longitudinal vortex acts to restrict the movement of the interacting vortex to spanwise direction. Therefore the margin of optimum height of the vortex generators pair is narrow.

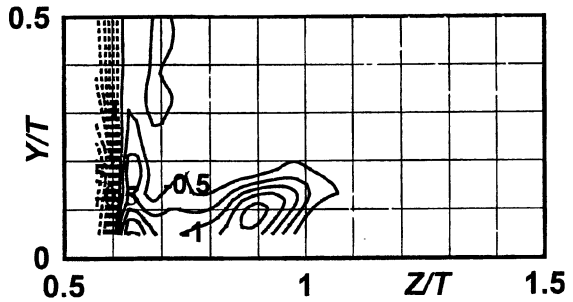

(a) non-*VG*

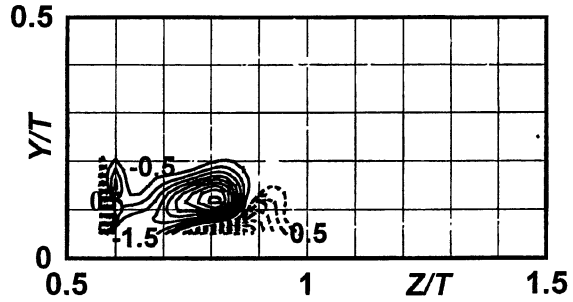

(b) *CFUC* (*H/T* = 0.17, *S/T* = 0.67)

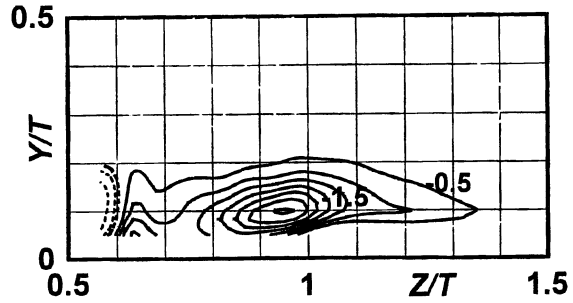

(c) *CFDC* (*H/T* = 0.17, *S/T* = 0.67)

Fig. 9 Contours of streamwise vorticity $\Omega_x T/U_r$ (*X/C* = 0.3)

REFERENCES

Devenport, W. J. and Simpson, R. L., 1990, "Time-Dependent and Time-Averaged Turbulent Structure Near the Nose of a Wing-Body Junction," J. Fluid Mech., 210, 23 – 55.

Eckerle, W. A. and Awad, J. K., 1991, "Effect of Freestream Velocity on the Three-Dimensional Separated Flow Region in Front of a Cylinder," J. ASME, Fluids Engineering, 113, 37 – 44.

Fleming, J. L., Simpson, R. L., Cowling, J. E. and Devenport, W. J., 1993, "An Experimental Study of a Turbulent Wing-Body Junction and Wake Flow," Exp. in Fluids, 14, 366 – 378.

Kubendran, L. R., McMahon, H. M., and Hubbartt, J. E., 1986, "Turbulent Flow around a Wing/Fuselage Type Juncture," AIAA J., 24 – 9, 1447 – 1452.

Shabaka, I. M. M. A. and Bradshaw, P., 1981, "Turbulent Flow Measurements in an Idealized Wing-Body Junction," AIAA J., 19, 131 – 142

Mehta, R. D., 1984, "Effect of Wing Nose Shape on the Flow in a Wing/Body Junction," Aeronaut. J., 88, 456 – 460.

Pauley, W. R. and Eaton, J, K., 1988, "Experimental Study of the Development of Longitudinal Vortex Pairs Embedded in a Turbulent Boundary Layer, "AIAA J., 26 – 7, 816 – 823.

Pauley, W. R. and Eaton, J, K., 1988, "The Fluid Dynamics and Heat Transfer Effects of Streamwise Vortices Embedded in a Turbulent Boundary Layer," Stanford University Report, MD – 51.

Shizawa, T., Eaton, J. K., 1992, "Turbulence Measurements for a Longitudinal Vortex Interacting with a Three-Dimensional Turbulent Boundary Layer," AIAA J., 30 – 1, 49 – 55.

Shizawa, T., Honami, S and Yamamoto, M., 1996, "Experimental Study of Horseshoe Vortex at Wing/Body Junction with Attack Angle by Triple Hot-Wire," AIAA Paper 96 – 0323.